ARTICLE OPEN

Check for updates

Many-body localization in the infinite-interaction limit and the discontinuous eigenstate phase transition

Chun Chen[1,2]✉, Yan Chen[3]✉ and Xiaoqun Wang[1,4,5,6]✉

We study many-body localization (MBL) in a spin-chain model mimicking the Rydberg-blockade quantum simulator with infinite-strength projection and moderate quasiperiodic modulation. Employing exact diagonalization, Krylov-typicality technique, and time-evolving block decimation, we identify evidence for a constrained MBL phase stabilized by a pure quasirandom transverse field. Intriguingly, the constrained MBL transition may embody a discontinuous eigenstate phase transition, whose discontinuity nature significantly suppresses finite-size drifts that plague most numerical studies of conventional MBL transition. Through quantum dynamics, we find that rotating the modulated field from parallel toward perpendicular to the projection axis induces an eigenstate transition between diagonal and constrained MBL phases. The entanglement-entropy growth in constrained MBL follows a double-log form, whereas it changes to a power law in approaching the diagonal limit. By unveiling confined nonlocal effects in integrals of motion of constrained MBL, we show this insulating state is not a many-body Anderson insulator. Our predictions are testable in Rydberg experiments.

npj Quantum Information (2022)8:142 ; https://doi.org/10.1038/s41534-022-00654-9

INTRODUCTION

The framework of many-body localization lays its foundation on the noninteracting Anderson insulator[1] to address the quest of ergodicity breaking[2,3] and instability toward delocalization and eigenstate thermalization[4,5] under weak many-body interactions in low spatial dimensions[6,7].

This short-range, weak-interaction picture forms the backbone of conventional MBL. Nonetheless, it also raises a question of whether there can arise many-body non-Anderson localization in circumstances where interaction strengths are not weak but infinitely strong. See refs. [8–16] for different considerations on the uniform or random-interaction systems.

Phenomenologically, isolated many-body Anderson insulators may be describable by the emergent extensive set of local integrals of motion (LIOMs or ℓ-bits)[17–20], at least in one dimension (1D)[21]. Then, is it conceivable that localization persists but owing to restriction or frustration, the LIOM-based picture breaks down? It is known that finite interaction activates more resonance channels for dephasing, so it is expected to suppress localization. In this regard, a better and affirmative route to achieving the unconventional MBL might be associated with the presence of restriction or frustration, for instance, in disordered Rydberg-blockade chains[22,23], where, as a consequence of strong, coherent dipole-dipole van der Waals repulsions, two nearest-neighboring Rydberg atoms cannot be simultaneously excited. This energy-constrained dynamics is modeled by a projection action of infinite strength.

Specifically, would there be a singular boundary separating different phases of MBL due to abrupt distortion rather than a progressive dressing of ℓ-bits?

MBL phase and MBL transition are two interdependent topics central to ergodicity breaking in statistical mechanics. Recently, there is a debate questioning whether MBL is a viable state in the thermodynamic limit. The issue stems from the strong finite-size drift of the MBL-thermal phase boundary seen in nearly all numerical scaling analyses of small chains[24–38]. Because the critical disorder strength keeps shifting toward infinity under the increase of the system's size, it was inferred that no MBL transition occurs within these models such that MBL might be a finite-size crossover phenomenon that ultimately gives way to the normal process of thermalization.

What about the nature of MBL transition in the presence of infinite interparticle interaction?

Counterintuitively, we find through solving a concrete lattice model that the eigenstate transition between MBL and thermal regimes may contrastingly be discontinuous when the (off-diagonal) constrained limit is taken, a feature probably enabled by the infinite interaction that considerably reduces the adverse effects of finite-size drifts at transition points. Consequently, both the stabilization of the unconventional constrained MBL state and the robustness of the diagonal MBL phase are strengthened.

RESULTS

The minimal model

The aforementioned physics might be visible in disordered and locally constrained chain models[23]. The simplest of such category takes the following archetypal form,

$$H_{\mathrm{qp}} = \sum_i \left(g_i \widetilde{X}_i + h_i \widetilde{Z}_i\right), \tag{1}$$

where $\widetilde{X}_i, \widetilde{Z}_i$ are projected Pauli matrices, $\widetilde{X}_i := P\sigma_i^x P$ and $\widetilde{Z}_i := P\sigma_i^z P$. The global operator $P := \prod_i \left(\frac{3+\sigma_i^z+\sigma_{i+1}^z-\sigma_i^z\sigma_{i+1}^z}{4}\right)$ prohibits motifs of $\downarrow\downarrow$-configuration over any adjacent sites, hence rendering the Hilbert space of model (1) locally constrained.

[1]Key Laboratory of Artificial Structures and Quantum Control (Ministry of Education), School of Physics and Astronomy, Shenyang National Laboratory for Materials Science, Shanghai Jiao Tong University, Shanghai 200240, China. [2]Max-Planck-Institut für Physik komplexer Systeme, Nöthnitzer Straße 38, 01187 Dresden, Germany. [3]Department of Physics and State Key Laboratory of Surface Physics, Fudan University, Shanghai 200433, China. [4]School of Physics, Zhejiang University, Hangzhou 310058 Zhejiang, China. [5]Tsung-Dao Lee Institute, Shanghai Jiao Tong University, Shanghai 200240, China. [6]Collaborative Innovation Center of Advanced Microstructures, Nanjing University, Nanjing 210093, China. ✉email: chunchen@sjtu.edu.cn; yanchen99@fudan.edu.cn; xiaoqunwang@zju.edu.cn

In ref. [23], we showed that a random version of the model (1) by quenched disorder exhibits tentative signatures of a constrained MBL (cMBL) phase; nevertheless, the Griffiths effect arising from the nearby transition impedes an unambiguous identification of this nonergodic eigenstate matter. In the current work, we improve our prior construction by conceiving an experiment-pertinent quasiperiodic constrained model with open and periodic boundary conditions (BCs), i.e., choosing[39–55]

$$g_i = g_x + W_x \cos(2\pi\xi i + \phi_x),\ h_i = W_z \cos(2\pi\xi i + \phi_z), \tag{2}$$

where the wavenumber $\xi = \sqrt{2}$ is irrational, $i = 1, \ldots, L$, and $\phi_x, \phi_z \in [-\pi, \pi)$ are different sample-dependent random overall phase shifts.

Since Hamiltonian (1) is real, time-reversal symmetry $T := K$ is preserved, giving rise to the Gaussian orthogonal ensemble (GOE) in phases obeying the eigenstate thermalization hypothesis (ETH)[56]. Additionally, when $W_z = 0$, there is a particle-hole symmetry $P := \prod_i \sigma_i^z$ that anticommutes with H_{qp}. To our knowledge, no discrete Abelian symmetry is present in Hamiltonian (1), so the possibility of a localization-protected spontaneous symmetry breaking[57] is excluded.

To manifest the fundamental interplay between finite tunable randomness and infinite interparticle interaction, we introduce hardcore boson operators $b^\dagger$, b on each site to describe the local pseudospin-$\frac{1}{2}$ system that emulates the Rydberg lattice gas with ground state $|g\rangle = |\uparrow\rangle$ and Rydberg excitation state $|r\rangle = |\downarrow\rangle$. In terms of hardcore bosons, the Pauli spin matrices can be couched as follows,

$$b^\dagger + b = |r\rangle\langle g| + |g\rangle\langle r| = |\downarrow\rangle\langle\uparrow| + |\uparrow\rangle\langle\downarrow| = \sigma^x, \tag{3}$$

$$b^\dagger b = n = |r\rangle\langle r| = |\downarrow\rangle\langle\downarrow| = \frac{(1-\sigma^z)}{2}, \tag{4}$$

where $n = 0, 1$ is the local occupation number of boson. Armed with the above expressions, Hamiltonian (1) can then be exactly mapped onto an array of neutral atoms in the Rydberg-blockade regime,

$$H_{\text{qp}} = H_x + H_z + H_V, \tag{5}$$

$$H_x = \sum_i g_i (b_i^\dagger + b_i), \tag{6}$$

$$H_z = \sum_i h_i (1 - 2n_i), \tag{7}$$

$$H_V = \sum_i V_1 n_i n_{i+1}, \quad V_1 = \infty. \tag{8}$$

Here g_i, h_i are proportional to onsite Rabi frequency and frequency detuning, respectively; the repulsive van der Waals interaction in Eq. (8) is truncated to retain only the nearest-neighbor interaction whose strength V_1 is lifted to infinity, producing a blockade radius of $a < R_b < 2a$. Clearly, H_x breaks the system's particle-number conservation, so the total energy is the only conserved quantity of the model.

Instructively, using spin operators in Eqs. (3) and (4), Hamiltonian (5) can also be recast into the standard mixed-field Ising model, for which Imbrie[21] proved in a mathematically quasiexact way the existence of many-body-generalized Anderson insulator under conditions of limited level attraction, weak-interaction strengths, and sufficiently strong disorders. In this regard, although we focus on the infinitely interacting version of such a particular model, the gained results bear the originality and significance to stimulate the research about many-body non-Anderson localization. Further, without H_V, $H_0 = H_x + H_z$ is a free Hamiltonian describing decoupled spins, each undergoing an independent Larmor precession about the local random fields.

Therefore, the constrained Rydberg atomic chain we consider consists of two pieces: a randomized but noninteracting term H_0 and a nearest-neighbor density-density interacting term H_V featured by an infinite repulsion.

Such a compact form with a single "spin-like" sector and the reduction of onsite Hilbert-space dimension from the usual value of 2 to the golden ratio $\phi = 1.618\ldots$ prompt us to regard the bare bones model (5) [or Eq. (1)] as the fundamental building block for studying the more generic constrained quantum systems, such as the t-J model.

Moreover, in light of the following commutation relations,

$$[H_x, H_V] \neq 0, \quad [H_z, H_V] = 0, \tag{9}$$

the constrained Hamiltonian (5) may accommodate two distinct physical extremes. (i) When $|W_z| \gg |g_x|$, $|W_x|$, the system approaches the diagonal limit during which the role of the infinite interaction is effectively minimized and the resulting diagonal MBL (dMBL) state represents a variant of many-body Anderson insulator with enhanced robustness[58]. To be pedantic, throughout this paper, we define the diagonal limit, an analog of Anderson limit, as specified by $h_i \neq 0$ and $g_i = 0$ in (1); while for dMBL, the analog of many-body Anderson localization, $|g_i|$, although perturbatively smaller than $|h_i|$, is not identically zero. (ii) In comparison, once $|g_x|$, $|W_x| \gg |W_z|$, the system enters the off-diagonal constrained limit—the true "infinite-interaction limit" quoted in the paper's title—where mutual impacts from modest randomness and infinite interaction are contrastingly maximized. Particularly, their constructive interplay gives rise to the sought infinite-interaction-facilitated MBL state, which is different from the "infinite-randomness-controlled" many-body Anderson localization stabilized in the opposite limit of weak interaction. Naïvely, no apparent duality would directly link these two.

It is worth stressing that the kinetic constraint was realized in a Rydberg-blockade chain[22] and the quasiperiodic modulation played a vital role in experiments[59–61] to achieve the first signature of MBL in unconstrained systems. Accordingly, the actual value of model (1) resides right in its high experimental relevance.

Throughout this paper, $W_x = 1$ sets the energy scale, i.e., the system is quasirandom, at least along the x direction.

Discontinuous cMBL-cETH transition: spectral analyses

The configuration averaged level-spacing ratio $[r]$ is the unique single-value quantity routinely adopted to characterize the dynamical states of matter. One defining feature of robust localization is the vanishing repulsion between contiguous gaps and the resulting Poisson distribution of

$$r_n := \frac{\min\{\delta_n, \delta_{n-1}\}}{\max\{\delta_n, \delta_{n-1}\}} \tag{10}$$

with mean $[r] = r_{\text{Poi}} \approx 0.386$ where $\delta_n := E_n - E_{n-1}$ assuming $\{E_n\}$ an ascending list of eigenvalues[31,32,62–64].

Figure 1a, b show the finite-size evolutions of $[r]$ as a function of g_x along the $W_z = 0$ axis. Via optimization of the ED algorithm targeting only the eigenvalues, we obtain the full eigenspectra of the chain for 1000 independent quasirandom samples up to system size $L = 26$ and the corresponding Hilbert-space dimension for such a single sample is 317811 under OBCs. (Parenthetically, the maximal chain length examined by a similar work[30] is also $L = 26$, as they used PBCs, the corresponding Hilbert-space dimension increases to 271443.) Within $0.5 < g_x \leqslant 1$, we find that $[r]$ steadily converges to r_{Poi} under the successive increase of L, verifying the stabilization of a desired cMBL phase.

The peculiarity of the quasiperiodic Rydberg chain may be rooted in the discontinuous eigenstate phase transition between cMBL and its nearby constrained ETH (cETH) phase. To pin down the potential discontinuity, we perform a finite-size scaling

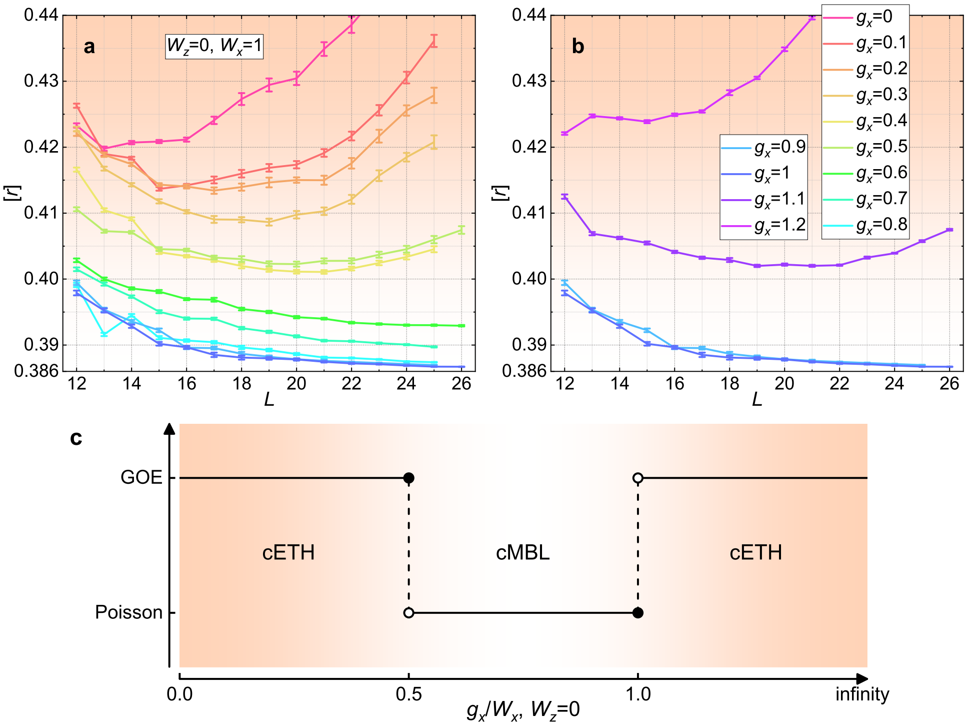

Fig. 1 Spectral diagnostics of the cMBL-cETH transition based on the scaling analysis of [*r*] using OBCs. The maximal chain length is pushed to $L = 26$. Under the constrained limit $W_z = 0$, the model's [*r*]-value forms a systematic trend in approaching r_{Poi} when $\frac{g_x}{W_x} \in (0.5, 1]$, demonstrating the realization of cMBL. Panels **a**, **b** show the proposed respective discontinuity for the left and right boundary of the transition. Panel **c** schematizes the ideal phase diagram along the (off-diagonal) constrained line in the thermodynamic limit where, as denoted by black dots, the chain at the left discontinuous transition point $g_x = 0.5$ is thermalized, whereas it remains fully localized at the right discontinuous transition point $g_x = 1$. This cMBL phase survives to finite $\frac{W_z}{W_x} \approx 0.5$, hence forming a dome separated from both the constrained thermal phase at leading g_x and the dMBL state at dominant W_z.

analysis of [*r*] by pushing the chain length to $L = 26$ and simultaneously selecting a compatibly high resolution $0.1W_x$ when tuning g_x. Figure 1a targets the left discontinuous transition point, from which one observes that for $0 \leqslant g_x \leqslant 0.5$, there exists a turning point of L beyond which [*r*] starts to increase continually toward GOE. More precisely, we find the following correspondence between g_x and its turning position of the length:

$$\begin{bmatrix} g_x \\ L \end{bmatrix} = \begin{bmatrix} 0 \\ 13 \end{bmatrix}; \begin{bmatrix} 0.1 \\ 15 \end{bmatrix}; \begin{bmatrix} 0.2 \\ 17 \end{bmatrix}; \begin{bmatrix} 0.3 \\ 19 \end{bmatrix}; \begin{bmatrix} 0.4 \\ 21 \end{bmatrix}; \begin{bmatrix} 0.5 \\ 20 \end{bmatrix}, \tag{11}$$

namely, the turning point of L increases along with g_x up to $g_x = 0.5$. Surprisingly, this trend terminates abruptly once $g_x > 0.5$. For instance, even after moving upward to $L = 26$, we find no signs of such a turning length for $g_x = 0.6$ and its [*r*]-value keeps rolling down toward r_{Poi}. This continual decrease of [*r*] becomes more transparent for $g_x = 0.7$, 0.8, 0.9, 1, which suggests the realization of cMBL within $g_x \in (0.5, 1]$. Therefore, the sharp distinction of the two trends induced by an incremental change of g_x indicates that the assumed discontinuity of the transition occurs at $g_x = 0.5$.

The discontinuity between the two contrasting trends showcases more vigorously at the right discontinuous transition point. As presented by Fig. 1b, although working on the small chain of $L = 26$, the [*r*]-value for $g_x = 1$ is already extremely close to the ideal value of the Poissonian distribution; while, in a striking comparison, the [*r*]-value for $g_x = 1.2$ appears to shoot up toward GOE at the very similar length scale. See also Fig. 3a, b. Crucially, the equality of [*r*] at $g_x = 0.9$, 1 and the finite jump of [*r*] at $g_x = 1.1$ comprise a vivid definition of discontinuity.

Based on the insights gained from extrapolating the scaling analysis of [*r*], we draw in Fig. 1c the schematic phase diagram of the quasirandom Rydberg chain in the thermodynamic limit. Here we exclusively focus on the constrained limit by fixing $W_z = 0$. After taking random averages, the sign of W_x makes no difference. Together with the unitary transformation rotated by σ_i^z, the sign of g_x does not matter either. One can thus take $W_x = 1$ and consider $\frac{g_x}{W_x} \in [0, +\infty)$ without loss of generality. There are several features of the phase diagram. (i) There exist only two eigenstate phases along the constrained line $W_z = 0$, the cMBL phase and the cETH phase. (ii) The cMBL phase occupies a finite interval $g_x \in (0.5, 1]$ and the cMBL-cETH transition is likely discontinuous whose transition points are located at the phase boundaries $g_x = \frac{1}{2}$ and $g_x = 1$. (iii) The system appears thermalized at $g_x = \frac{1}{2}$; while on $g_x = 1$, the chain maintains its full localization character. (iv) At the special point $g_x = 0$, where the relative randomness strength is infinite $W_x/g_x = \infty$, the chain is well within the cETH phase.

The robustness of cMBL implies the existence of dMBL in the thermodynamic limit, because adding another source of randomness can only enhance localization. In this sense, the constraint-induced delocalization reported by ref. [30] does not lead to contradictions but rather highlights the importance of cMBL as the state to foster dMBL. It also becomes clear about the necessity to include both terms of g_x and W_x on an equal footing to achieve the stabilization of localization in a generally constrained setting. Nonetheless, this type of randomness encapsulated by the term g_i is not the topic of ref. [30].

Transition points refined. We examine the postulated discontinuity of [*r*] at the transition points a bit further in Fig. 2, where by zooming in the left [panel a] and right [panel b] transition zones, we highlight the opposite scaling trends of [*r*] for the two g_x's that are close in magnitude. In accordance with the emergent integrability of cMBL, Fig. 2c, d show up to $L = 26$, the decrease and the convergence of [*r*] onto the Poisson value at $g_x = 0.6$, 1. The degree of discontinuity of

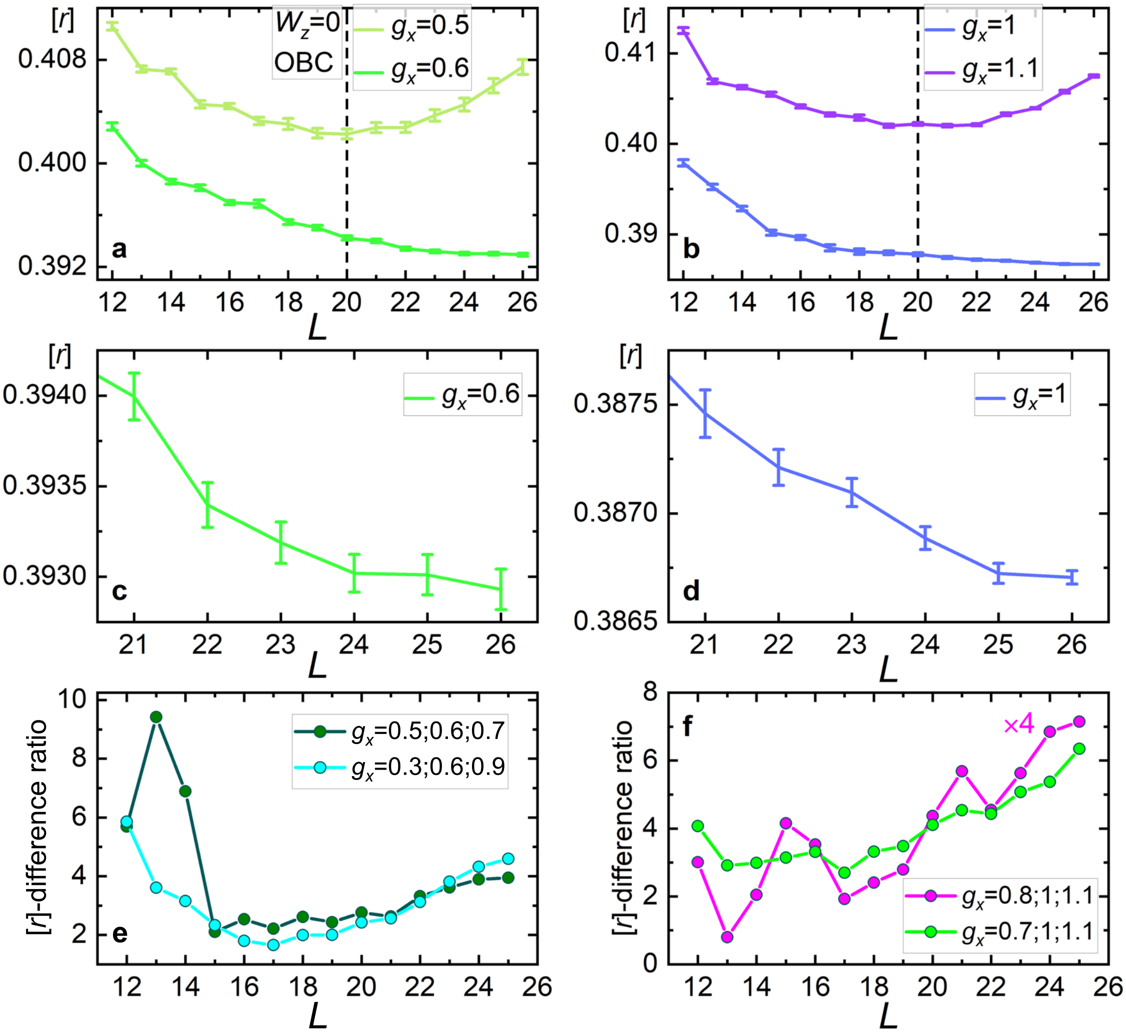

Fig. 2 [r] data at the left and right transition points. Dashed lines in **a**, **b** mark the lengths exceeding which the [r] values for $g_x = 0.5$, 1.1 begin to grow. By contrast, **c**, **d** show the monotonic decrease of [r] at $g_x = 0.6$, 1 toward r_{Poi}. All data are taken from Fig. 1 with $W_z = 0$. **e**, **f** plot the [r]-difference ratios near the two transition points to assess the sharpness of the discontinuity for the underlying transition.

the transition may be quantified in terms of the [r]-difference ratio defined by comparing the [r]-values at three adjacent g_x's, viz., with a particular L, for ordered $g_x = g_1$; g_2; g_3,

$$[r]\text{-difference ratio} := \frac{\max\{|[r](g_1)-[r](g_2)|, |[r](g_2)-[r](g_3)|\}}{\min\{|[r](g_1)-[r](g_2)|, |[r](g_2)-[r](g_3)|\}}. \tag{12}$$

For continuous transitions, the [r]-difference ratio is on the order of 1; whereas, if discontinuity arises, then it is predicted to diverge right at the transition once the thermodynamic limit is taken. By choosing four g_x-tuples involving the two transition points, we illustrate via Fig. 2e, f the growth of [r]-difference ratio above unity under the increase of L. Within the system sizes we probe, the degree of discontinuity on the right transition point appears stronger than that of the left one. This is attributed to the different eigenstate phases realized at these two transition points.

In Supplementary Note 1, we provide additional evidence to support the discontinuity of the cMBL-cETH transition via a direct comparison to the continuous change from ETH to MBL driven by purely diagonal disorders.

Purely random point. In phase diagram Fig. 1c, the point $(\frac{g_x}{W_x} = 0, \frac{W_z}{W_x} = 0)$ bears multiple physical meanings. (i) It represents the purely random limit. Figure 3a evidences that in the presence of infinite interaction, the purely random Rydberg chain likely reaches full thermalization under the constrained limit with no signature of localization. This contrasts to the full localization at $(\frac{g_x}{W_x} = 1, \frac{W_z}{W_x} = 0)$ as is displayed in Fig. 3b. (ii) An implication of (i) pertains to the probable connection between the existence of cMBL and the discontinuity of the cMBL-cETH transition. This is because if assume the cMBL transition is continuous, then the inevitable finite-size drifts would dominate and consequently cast cMBL into doubt. (iii) When $W_z = 0$, by implementing the unitary symmetry involving σ_i^z to alter the sign of g_i combined with an energy-scale redefinition, one can exactly map $(\frac{g_x}{W_x} = 0, \frac{W_z}{W_x} = 0)$ onto $(\frac{g_x}{W_x} = 1, \frac{W_z}{W_x} = 0)$; however, this mapping is valid if the randomness is quench disorder and obeys the uniform box distribution[23]. For quasiperiodic randomness, such a formal equivalence breaks down, but our numerical data hint that $(\frac{g_x}{W_x} = 0, \frac{W_z}{W_x} = 0)$ might still be equivalent to a point infinitesimally close to but different from $(\frac{g_x}{W_x} = 1, \frac{W_z}{W_x} = 0)$. Symbolically, it reads $(\frac{g_x}{W_x} = 1 + 0^+, \frac{W_z}{W_x} = 0)$. This reasoning implies that the two disjoint cETH regions on the left and right side of the cMBL phase are physically equivalent, and the robustness of cMBL may thus be cemented by the significant degree of discontinuity of the transition at $g_x = 1$. In parallel, one can hypothesize that the

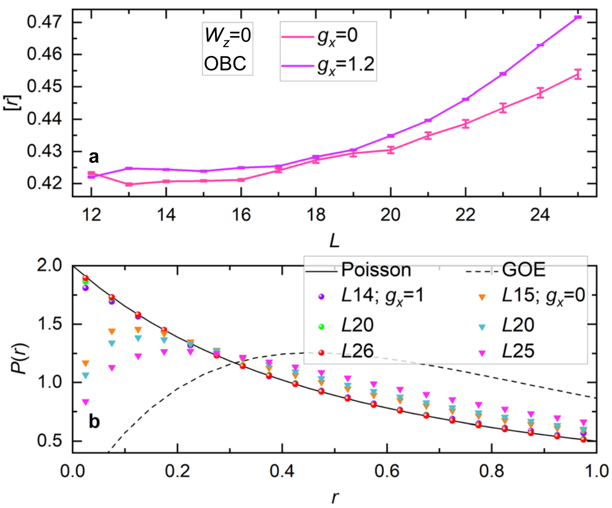

Fig. 3 Thermalization at a purely random point. **a** [*r*]-values of the chain for the two parameter sets ($g_x = 0$, $W_z = 0$) and ($g_x = 1.2$, $W_z = 0$). Both grow promptly toward the value of GOE with *L*, suggesting the system at both parametric points obeys ETH in the thermodynamic limit. **b** The probability distribution of the level-spacing ratio *P*(*r*) in cMBL (ensured by $g_x = 1$, $W_z = 0$), which closely traces the prediction of Poisson statistics [solid line, $P_{\mathrm{Poi}}(r) = 2/(1+r)^2$] under the increase of *L*, indicating the realization of a full MBL. By selecting $g_x = 0$, $W_z = 0$, the *P*(*r*) distribution switches to follow the Wigner surmise [dashed line, $P_{\mathrm{GOE}}(r) = (27/4)(r+r^2)/(1+r+r^2)^{5/2}$], signaling that thermalization sets in.

phase diagram for the quench-disordered Rydberg chain is identical to Fig. 1c, except that the black dot at $g_x = 1$ moves from Poisson to GOE. This conjecture overlooks the Griffiths rare-region effects and the ensuing avalanche-driven delocalization[65] in disordered models, which can be detrimental to cMBL phase and transition alike.

Continuous cMBL-dMBL transition: entanglement variances

The bipartite entanglement entropy $[S_{\mathrm{vN}}]$ is another useful proxy for analyzing MBL as is $[r]$[31,32,66]. For each eigenstate $|\psi_n\rangle$, the half-chain von Neumann entropy is defined by $S_{\mathrm{vN}} := -Tr_R[\rho_R \log_2 \rho_R]$ where $\rho_R := Tr_L[|\psi_n\rangle\langle\psi_n|]$ is the reduced density matrix of the right half chain. Using ED, we compute S_{vN} for the entire eigenspectrum of a given sample and obtain $[S_{\mathrm{vN}}]$ after averaging over all available eigenstates for more than 1000 independent quasirandom realizations.

Figure 4a, b show the respective evolutions of $[r]$ and $[S_{\mathrm{vN}}]/S_{\mathrm{P}}$ as a function of W_z along the $g_x = 1$ axis. Upon increasing *L*, both $[r]$ and $[S_{\mathrm{vN}}]/S_{\mathrm{P}}$ converge to a flattening curve centering around r_{Poi} and 0, respectively, demonstrating the system retains full localization as W_z varies from cMBL to dMBL. Because no discontinuity is found in $[r]$ and $[S_{\mathrm{vN}}]/S_{\mathrm{P}}$, the change of the phase structure is expected to be continuous. Here $[S_{\mathrm{vN}}]$ is normalized with respect to the Page value of the thermal entropy[67] whose estimate suitable for constrained circumstance equals $S_{\mathrm{P}} \approx \log_2(F_{L/2+2}) - 1/(2\ln 2)$ where the half-chain Hilbert-space dimension equals the Fibonacci number $F_{L/2+2}$[23].

Differing in entanglement patterns, continuous transition between unconstrained MBL and ETH phases can be probed via the standard deviation of S_{vN}. As first demonstrated by refs. [68,69], the explicit dependence of S_{vN} on eigenstate wavefunction ("*E*"), randomized sample ("*s*"), and partition cut ("*c*") brings about three measures for the quantity. In the following, we adopt this strategy for the continuous cMBL-dMBL transition. We borrow the convention of ref. [23], viz., using $[\ldots]_{E/s/c}$ to denote the respective averages over the eigenspectrum entirety, all samples, and all cuts with the unspecified subscripts holding fixed. Similar definitions carry over to the standard deviations $\Delta_{E/s/c}(\ldots)$.

In accordance with the continuous changes of $[r]$ and $[S_{\mathrm{vN}}]/S_{\mathrm{P}}$ in Fig. 4a, b, 4c illustrates the subvolume scaling law of $[\Delta_E[S_{\mathrm{vN}}]_c]_s/S_{\mathrm{P}}$, the state-to-state intrasample deviation of S_{vN}, upon raising *L* and its overall smooth lineshape as a function of W_z. Likewise, the cut-to-cut entanglement-entropy deviation, as given in Fig. 4d, exhibits the qualitatively consistent tendency for the same evolution between the two MBLs.

By comparison, albeit being less prominent for quasiperiodic arrangements, the sample-to-sample entanglement-deviation curve presented by Fig. 4e gives the indication of an emergent peak around $\frac{W_z}{W_x} = 1$, hinting that the rise of W_z at fixed $g_x = 1$ may drive a continuous transition from cMBL toward dMBL. Intuitively, although both MBLs are dominantly constituted by area-law entangled eigenstates, on finite-length chains, the rates of how they approach the area scaling law may differ in magnitude and form, which potentially allows for the entropy variance across different samples near the phase boundary. Nonetheless, in view of the fact that the absolute value of the deviation is not pronounced and the shape of the curve keeps flattening, it is possible that cMBL and dMBL might vaguely be distinguishable from pure static diagnostics.

Eigenstate transition from entanglement growth

Alternatively, the qualitative difference between cMBL and dMBL can be demonstrated from the angle of real-time evolution of entanglement. Notably, we find an eigenstate transition between these two dynamical regimes in the numerical quantum quench experiments.

We use two quantities, the bipartite entanglement entropy and the quantum Fisher information (QFI). The initial state is randomly selected from the complete basis of nonentangled product states of σ_i^z-spins that respects the local constraint. For each *L*, we generate more than 1000 random pairs of (ϕ_x, ϕ_z) for the Hamiltonian, and for each quasiperiodic arrangement, we let the chain evolve and calculate S_{vN}, QFI by ED and TEBD[70] before averaging (see methods section).

Figure 5a compiles time evolutions of $[S_{\mathrm{vN}}]$ along the cut $g_x = 1$ with ascending W_z at $L = 20$ in a log-log format. The salient feature there is the qualitative functional change in the time-evolution profiles. This eigenstate transition is elaborated by Fig. 5c and e, where we focus on the entanglement growth deep inside cMBL and dMBL, respectively. For concreteness, after a transient period $t \lesssim 1$ of the initial development, $[S_{\mathrm{vN}}]$ in dMBL grows steadily as a power law of *t* [with an exponent (≈0.1)] within the next prolonged window (up to $t \approx 10^{14}$ at $L = 20$) but its saturated value is far less than the thermal entropy $S_T \approx \log_2(F_{2+L/2}) - 1/(2\ln 2) - 0.06$[23]. In stark comparison, the growth of $[S_{\mathrm{vN}}]$ in cMBL as displayed by Fig. 5c follows a different functional form: within $10^2 \lesssim t \lesssim 10^9$ at $L = 20$, the double-log function fits the entropy data reasonably well. Moreover, the equilibrated $[S_{\mathrm{vN}}]$ reaches a subthermal value in cMBL and obeys a volume scaling law.

Experimentally, the QFI, which sets the lower bound of entanglement, was measured in trapped-ion chain[71] to witness entanglement growth under the interplay between MBL and long-range interactions. Following[71], we start from Néel states in even chains, $|\psi(t=0)\rangle = |\downarrow\uparrow\ \ldots\ \downarrow\uparrow\rangle$, characterized by a staggered $\mathbb{Z}_2$ spin-imbalance operator, $I := \frac{1}{L}\sum_{i=1}^{L}(-1)^i\sigma_i^z$, then the associated QFI density reduces to the connected correlation function of *I*, $f_Q(t) = 4L(\langle\psi(t)|I^2|\psi(t)\rangle - \langle\psi(t)|I|\psi(t)\rangle^2)$, which links multipartite entanglement to the fluctuations encoded in measurable quantum correlators. Figure 5b is a semi-log plot of averaged $[f_Q]$ along the line $g_x = 1$ with different W_z color-coded the same way as in Fig. 5a. Likewise, the notable change in the functional form of $[f_Q]$ echoes the same cMBL-dMBL eigenstate transition. Specifically,

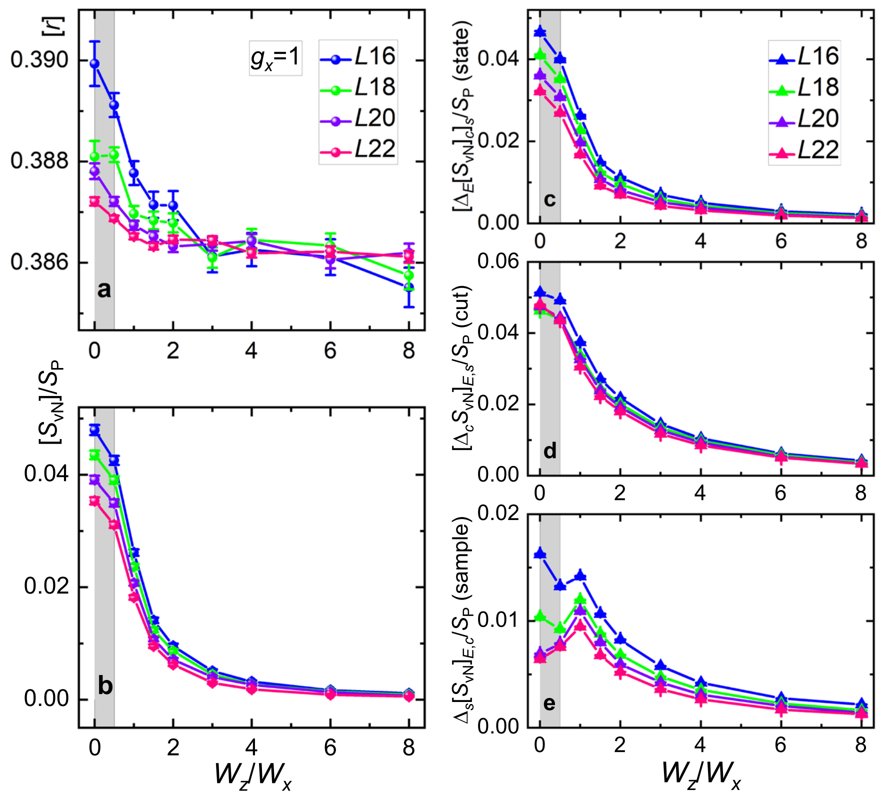

Fig. 4 Static diagnostics of the continuous cMBL-dMBL transition using the variance of S_{vN} under OBCs. a, **b** Finite-size scaling analyses show that at fixed $\frac{g_x}{W_x} = 1$, $[r]$ and $[S_{vN}]/S_P$ stay around r_{Poi} and 0 under the adjustment of W_z from cMBL toward dMBL. No discontinuity is observed. **c** The intrasample deviation of the entanglement entropy across the entirety of the eigenspectrum, $[\Delta_E[S_{vN}]_c]_s/S_P$. The accompanying cut-to-cut and sample-to-sample parsings of this entropy deviation are plotted by **d** and **e**, respectively. The peak forming at $\frac{W_z}{W_x} = 1$ in **e** points toward a transition between cMBL (shaded) and dMBL.

Fig. 5d shows that the long-time growth of $[f_Q]$ in cMBL matches a triple-log form, which reinforces the double-log fit of $[S_{vN}]$ in c. The parallel relation between $[S_{vN}]$ and $[f_Q]$ carries over to the dMBL phase, where the power-law growth of $[S_{vN}]$ in e transforms into a logarithmic growth of $[f_Q]$ in f.

Table 1 recaps the cMBL-dMBL distinction in the fundamental dynamical aspects of entanglement and its witness.

To supplement the ED simulation in main panels, we employ TEBD and matrix-product-operator techniques to verify the cMBL-dMBL transition in a larger system size $L = 28$. A 4th-order Suzuki-Trotter decomposition is implemented at a maximal time step of unity (the appropriate time step is set by the inverse mean gap and for large W_z, we find that a smaller time step of about 0.1 is needed, but as the entanglement growth deep inside dMBL is very slow, TEBD maintains its efficiency at this small time step), and the truncation error per step is controlled lower than 10^{-6} by selecting a large bond-dimension threshold 1500. We check that for $t \lessapprox 10^3$, the accumulated total truncation error in typical quasirandom samples is well below 10^{-5}. The corresponding results and the fits are consistently presented in the insets of Fig. 5. However, due to entanglement accumulation, matrix-product-state algorithms of this type retain effectiveness within limited time scales ($t \lessapprox 10^3$).

Double-log entanglement growth. As a refinement, Fig. 6a, c manifest that for cMBL, the double-log fitting function $\log\log(t)$ matches the $[S_{vN}]$ data significantly better than the single-log fitting function $\log(t)$, the hallmark of the unconstrained MBL[72–75]. Likewise, Fig. 6b, d show the entanglement data for larger chain's length $L = 22$ with the model parameters, $\frac{g_x}{W_x} = 1, \frac{W_z}{W_x} = 0$, intact. As indicated by pairs of dashed lines there, it is estimated that the duration that best traces the double-log fit increases progressively from $t \in (100, 10^{7.5})$ $[\Delta t \approx 3.162 \times 10^7]$ in system $L = 18$ to $t \in (360, 10^9)$ $[\Delta t \approx 10^9]$ in system $L = 22$, thus supporting the double-log entanglement buildup in cMBL.

Triple-log rise of QFI. Complementarily, Fig. 6e, f reproduce the temporal evolutions of $[f_Q]$ for two chosen parameters $W_z = 0, 0.5$ on longer chains. The fits on top of data from various lengths corroborate the speculation that this triple-log growth of $[f_Q]$ may comprise a feature shared within the dome of cMBL. Similar to Fig. 6a, b, here we resort to ED and raise the maximum open-chain size to $L = 22$.

Eigenstate transition from transport

Additionally, there are marked differences between cMBL and dMBL, as reflected through the chain's relaxation from the prepared Néel state and the spread of initialized local energy inhomogeneity. In accordance with the time evolution of $[S_{vN}]$ and $[f_Q]$, the decay of $I(t) := \langle \psi(t)|I|\psi(t) \rangle$ is examined in Fig. 7a. Apart from a quick suppression during $t \lessapprox 1$, both MBLs relax to a steady state with finite magnetization. They thus retain remnants of the initial spin configuration in contrast to the thermal phase where $[I(t)]$ vanishes irrevocably. Notice that under the increase of W_z, the frozen moment $[I_\infty]$ at infinite t develops monotonously from ~0.5 in cMBL up to ~0.9 in dMBL; before equilibration, the intermediate oscillation of $[I(t)]$ is also damped more severely in dMBL than in (off-diagonal) cMBL.

Following[76], the energy transport of the constrained model is scrutinized by monitoring the spread of a local energy

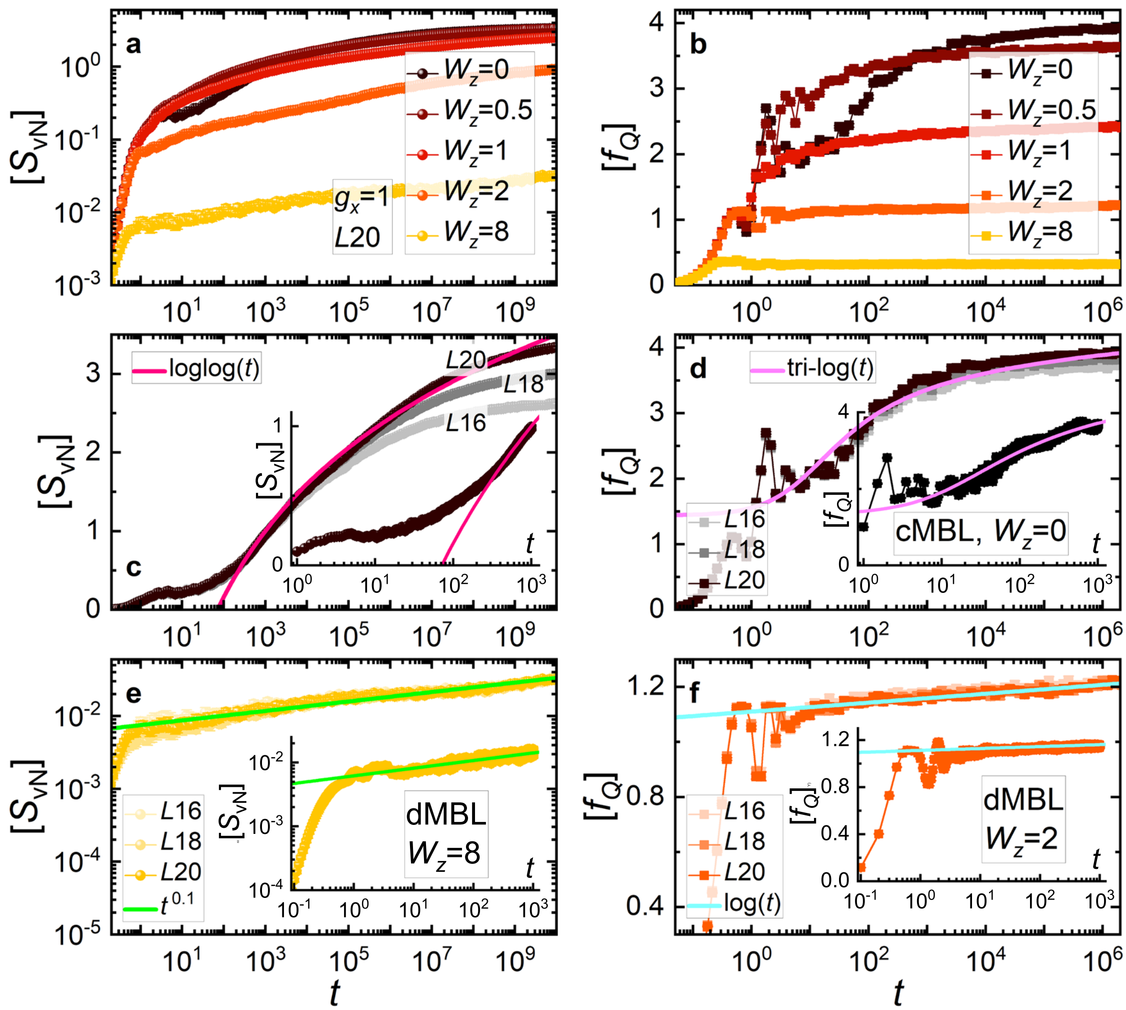

Fig. 5 cMBL-dMBL transition in dynamics with OBCs and fixed $g_x = 1$. The maximum chain length in ED is $L = 20$. The top row (**a**, **b**) summarizes functional changes of the growth of $[S_{vN}]$ and $[f_Q]$ as a function of W_z. Fits in the middle row (**c**, **d**) suggest that for cMBL at $W_z = 0$, the entanglement (QFI) growth follows a double (triple) logarithmic form. The bottom row (**e**, **f**) targets the dynamics of dMBL at large W_z: consistent with the logarithmic rise of $[f_Q]$, $[S_{vN}]$ grows as a power law of t in dMBL. The four insets of **c**–**f** present the corresponding TEBD results of $L = 28$.

Table 1. Hierarchies of dynamic characteristics encompassing constrained, unconstrained, and diagonal MBL phases.

	$[S_{vN}]$	[Quantum Fisher Info.]
cMBL	$\log\log(t)$	$\log\log\log(t)$
uMBL	$\log(t)$	$\log\log(t)$
dMBL	t^{α}	$\log(t)$

inhomogeneity initialized on the central site of an odd chain at infinite temperature, i.e., the system's initial density matrix assumes $\rho(t=0) = \frac{1}{\dim\mathcal{H}}(\mathbb{1} + \varepsilon\widetilde{X}_{\frac{L+1}{2}})$, where $\dim\mathcal{H}$ the dimension of projected Hilbert space and ε the disturbance of energy on site $i_c := (L+1)/2$. The quantity measuring the effective distance ε travels is $R(t) := \frac{1}{Tr\left[\widetilde{\rho}(t)H_{\rm qp}\right]}\sum_{i=1}^{L}\{|i - i_c|Tr[\widetilde{\rho}(t)H_i]\}$, where $H_i := g_i\widetilde{X}_i + h_i\widetilde{Z}_i$ and the time-independent background is subtracted via inserting $\widetilde{\rho}(t=0) := \frac{1}{\dim\mathcal{H}}\varepsilon\widetilde{X}_{\frac{L+1}{2}}$. As per ETH, ε is eventually smeared uniformly over the chain by unitary time evolution and in that circumstance $[R(t=\infty)] \approx L/4$. Figure 7b contrasts the behavior of $[R(t)]$ between cMBL and dMBL. Concretely, for dMBL, $[R]$ stays vanishingly small; thereby, ε remains confined to i_c and shows no diffusion toward infinite t. In comparison, as the consequence of a fast expansion within $t \lessapprox 100$, largely due to contributions from nearest and next-nearest neighbors, ε spreads over a finite range of the chain in cMBL. Here, however, the saturated value $[R_\infty]$ after an oscillatory relaxation remains subthermal.

Integrals of motion and dynamical order parameters

The key distinction between cMBL and dMBL can be further resolved by studying the long-time limit of the spatial distribution of the energy-inhomogeneity propagation. We utilize three quantities to access this information complementarily.

(i) For each quasirandom realization, we parse the definition of $R(t)$ as per the site index, $\varepsilon_i(t) := \frac{Tr\left[\widetilde{\rho}(t)H_i\right]}{Tr\left[\widetilde{\rho}(t)H_{\rm qp}\right]}$, which measures in percentage the extra energy on position i with respect to the total conserved perturbation ε. Observing that ε_i approaches a constant $\varepsilon_{i,\infty}$ at infinite t, one might implement the trick[77], $\lim_{T\to\infty}\frac{1}{T}\int_0^T O(t)dt \approx \sum_n \langle n|O|n\rangle|n\rangle\langle n|$, to extract its value with the

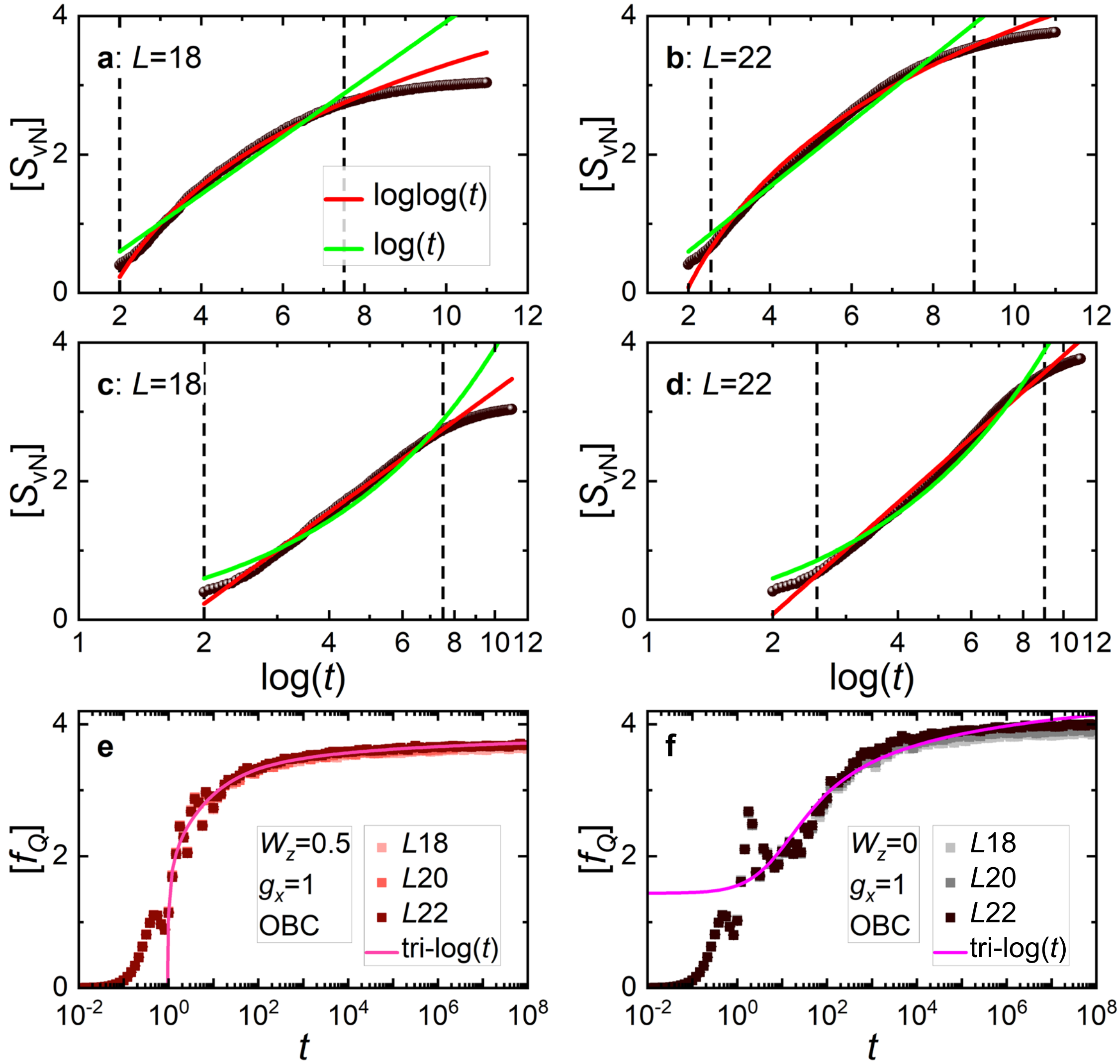

Fig. 6 Refined data analyses. a, **c** A replot of $[S_{\rm vN}]$ in cMBL (stabilized by $\frac{g_x}{W_x}=1, \frac{W_z}{W_x}=0$) on an open chain of $L=18$ but now fitted by two different types of functions: $\log\log(t)$ and $\log(t)$. The lower panel is the same as the upper one but in a semi-log format. Apparently, $\log\log(t)$ gives the better fit. **b**, **d** The $[S_{\rm vN}]$ data of a long open chain $L=22$ with the same model parameters. In each panel, the time interval that matches the double-log fit is marked by two dashed lines. Noticeably, this time window broadens from $t\in(100, 10^{7.5})$ for $L=18$ to $t\in(360, 10^9)$ for $L=22$. **e**, **f** Temporal growth of $[f_Q]$ at two representative points inside the cMBL dome using longer chains. Both can be captured by the triple-log functions of time. **e** corresponds to $W_z=0.5$, while **f** repeats Fig. 5d for comparison.

aid of randomness,

$$\varepsilon_{i,\infty} := \varepsilon_i(t\to\infty) \approx \frac{\sum_n \langle n|\widetilde{X}_{\frac{L+1}{2}}|n\rangle\langle n|H_i|n\rangle}{\sum_n E_n\langle n|\widetilde{X}_{\frac{L+1}{2}}|n\rangle}, \tag{13}$$

where $\{|n\rangle\}$ comprises an eigenbasis satisfying $H_{\rm qp}|n\rangle = E_n|n\rangle$. Evidently, the profile of $\{\varepsilon_{i,\infty}\}$ bears information pertaining to the local structure of integrals of motion (IOMs).

(ii) The summation of $\varepsilon_{i,\infty}$ weighted by the separation returns the equilibrated value of the effective traveling distance, $R_\infty = \sum_{i=1}^{L}(|i-i_c|\cdot\varepsilon_{i,\infty})$.

(iii) Viewing that the contribution from i_c, i.e., the return probability, is missing from R_∞, one can define $\varepsilon_{i_c,\infty}$ as the residual energy density on the release place, $\varepsilon_{\rm res} := \varepsilon_{\frac{L+1}{2},\infty}$.

All three quantities defined above are used to distinguish ETH and MBL. Here we show that they are also the dynamical "order parameters" to differentiate between the cMBL and dMBL regimes and identify the transition point therein.

LIOMs and positive definiteness of dMBL

Despite the central status of LIOMs in disorder-induced MBL[17–20], LIOMs in unconstrained aperiodic MBL systems have received attention only recently[47,51]. Ref. [47] constructed LIOMs of MBL as time-averaged local operators for interacting fermions subject to aperiodic potentials. They found that in this circumstance, ℓ-bits remain localized even at the vicinity of the quasiperiodic MBL transition. Likewise, upon continuous unitary transforms, ref. [51] computed the real-space support of LIOM in quasirandomness-induced MBL and revealed that the effective interactions between LIOMs exhibit features inherited from the underlying aperiodic potential. Interestingly, both works pointed to the weaker finite-size effects in aperiodic modulations than in truly disordered arrangements. Exploiting the instability of LIOMs, they also found that the associated MBL transition may occur at a higher critical quasirandom strength than previously estimated[40].

Before proceeding to numerics, let us gain some understanding of dMBL within the LIOM framework. The first step forward is to introduce $\breve{Z}_i := \mathcal{P}_{i+1}\widetilde{Z}_i\mathcal{P}_{i-1}$ where $\mathcal{P}_i := \frac{1}{2}(\mathbb{1}+\sigma_i^z)$ as the building blocks of constrained ℓ-bits. The convenience of $\breve{Z}_i$ stems from

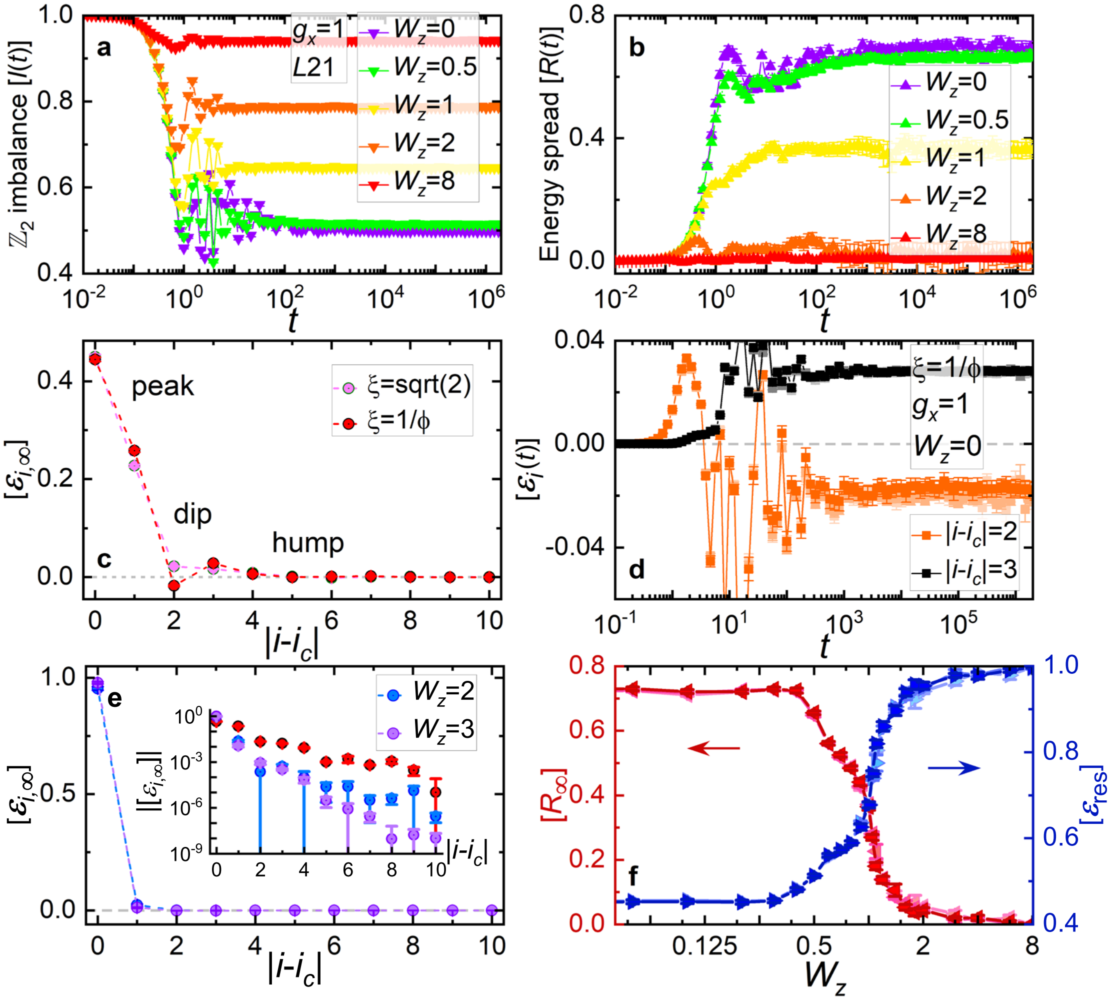

Fig. 7 cMBL-dMBL transition in transport with PBCs and fixed $g_x = 1$, $L = 21$. a, b Time evolution of the $\mathbb{Z}_2$ antiferromagnetic imbalance $[I(t)]$ and the energy spread $[R(t)]$ as a function of W_z. **c** exemplifies the peak-dip-hump lineshape of $[\varepsilon_{i,\infty}]$ in cMBL for two irrational wavenumbers ξ. One set of time-profiles of $[\varepsilon_{i_c\pm2,3}(t)]$ that characterizes the nonmonotonicity of the dip-hump structure is given by **d**. **e** shows the lineshape of $[\varepsilon_{i,\infty}]$ in dMBL; the exponential decay can be seen from the semi-log inset wherein the cMBL data (pink dots) are overlaid for comparison. **f** The changes in dynamic `\lq order parameters' $[R_\infty]$ and $[\varepsilon_{\rm res}]$ under the tuning of W_z signal the transition between cMBL and dMBL. Light to solid colors in **d**, **f** correspond to $L = 17, 19, 21$.

$Tr\breve{Z}_i = 0$, which contrasts to $Tr\widetilde{Z}_i > 0$, thereby $\breve{Z}_i$ behaves like a spin free of restrictions. Following[23], it can be proved that as long as $W_z \gg g_x + W_x$, the set of tensor-product operators $\mathcal{I}_L := \{\mathcal{Z}_{i_1} \otimes \cdots \otimes \mathcal{Z}_{i_k}\}$ fulfilling $1 \leqslant i_1 \leqslant i_2 \leqslant \cdots i_k \leqslant L$, $i_{a+1} \neq i_a$, $1 \leqslant k \leqslant \frac{L+1}{2}$ may be constructed as a complete, mutually commuting, and linearly-independent basis to express any nontrivial operators that commute with $H_{\rm qp}$; in terms of quasilocal unitaries, $\mathcal{Z}_{i_a} \approx U\breve{Z}_{i_a}U^\dagger$. This is because the set of states $\{|\mathcal{Z}_{i_1}\mathcal{Z}_{i_2}\cdots\mathcal{Z}_{i_k}\rangle\}$ derived from $\mathcal{I}_L$ reproduces faithfully the effective eigenbasis of projected Hilbert space for dMBL. Accordingly, the IOM in Eq. (13) is recast into

$$\text{dMBL}: \sum_n \langle n|\widetilde{X}_i|n\rangle |n\rangle\langle n| \approx \sum_{m=0}^{\frac{L-1}{2}} \sum_r V_{r,m}^{[i]} \widehat{\mathcal{O}}_{r,m}^{[i]}, \tag{14}$$

where $\widehat{\mathcal{O}}_{r,m}^{[i]}$ denotes the element of $\mathcal{I}_L$ possessing the support on site i (i.e., contains $\mathcal{Z}_i$) and whose furthest boundary from i is of distance m. The nonidentical members comprising this specified subset are labeled by r. Besides the finite support of $\mathcal{Z}_i$, the key property that promotes $\sum_n \langle n|\widetilde{X}_i|n\rangle|n\rangle\langle n|$ to the LIOM of dMBL is the locality condition of its real coefficients, i.e., $V_{r,m}^{[i]} \sim e^{-m/\zeta}$. In terms of LIOM representation, the universal Hamiltonian governing the dynamics of dMBL may assume the following form, $H_{\rm qp}^{\rm dMBL} = \sum_i \widetilde{h}_i \mathcal{Z}_i + \sum_k \sum_{i_1\ldots i_k} J_{i_1\ldots i_k} \mathcal{Z}_{i_1}\mathcal{Z}_{i_2}\cdots\mathcal{Z}_{i_k}$, where from Fig. 5e, f, it is feasible to infer $J_{i_1\ldots i_k} \sim |i_k - i_1|^{-1/\alpha} \cdot \phi^{-|i_k - i_1|}$, which decays as an exponentially-suppressed power law of LIOMs' separation. Here, α is the same exponent in Table 1 and ϕ is the golden ratio.

Being the trace of a product of two IOMs, one consequence of Eq. (14) is the positive definiteness of the averaged $[\varepsilon_{i,\infty}]$ featured by an exponential decay in space. Figure 7e illustrates that this is the case even when $W_z \approx g_x + W_x$.

Peak, dip, hump in cMBL

Now we are in the position to highlight the peak-dip-hump structure and the occurrence of negativity in $[\varepsilon_{i,\infty}]$ [see Fig. 7c, d] as the peculiarities of cMBL that distinguish it from both dMBL and unconstrained MBL (uMBL) by the presence of pronounced nonlocal correlations. The unambiguous negativity of $[\varepsilon_{i_c\pm2}]$ in Fig. 7c and the nonmonotonicity of $[\varepsilon_{i_c\pm2,3}]$ in Fig. 7d point to the insufficiency of Eq. (14) when addressing the cMBL phase from the dMBL side. Especially, they highlight the dynamical consequence that in cMBL the correlation between the center site (where the initial energy inhomogeneity locates) and its third nearest neighbors might be stronger than that for its second nearest neighbors, because phenomenologically the net energy current flowing into the second nearest-neighboring sites could appear noticeably less than that flows out. To remedy the inconsistency, we propose as a scenario that the missing pieces may come from the terms in $\mathcal{I}_L$ that are nonlocal with respect to i, viz., their support on i vanishes, hence, for cMBL, $\sum_n \langle n|\widetilde{X}_i|n\rangle|n\rangle\langle n| \approx \sum_{m=0}^{\frac{L-1}{2}} \sum_{r,\bar{r}} (V_{r,m}^{[i]} \widehat{\mathcal{O}}_{r,m}^{[i]} + V_{\bar{r},m}^{\overline{[i]}} \widehat{\mathcal{O}}_{\bar{r},m}^{\overline{[i]}})$. The superscript $\overline{[i]}$ signifies the absence of $\mathcal{Z}_i$ in the associated expansion. Under the successive decrease of W_z, it is anticipated that the weights $V_{\bar{r},m}^{\overline{[i]}}$ of small m grow significantly such that a finite-size core centered at i forms wherein nonlocal correlated contributions, albeit confined, become predominant. On the contrary, for those m beyond the core, the importance of $V_{\bar{r},m}^{\overline{[i]}}$ diminishes sharply so that the rapid decay tail and the overall signatures of localization are well maintained.

Alternatively, the core formation may be monitored by $[R_\infty]$ and $[\varepsilon_{\rm res}]$. Figure 7f illustrates that the duo constitutes the desired 'order parameters' from quantum dynamics that take values zero and unity in dMBL and saturate to nontrivial plateaus in cMBL. The critical W_z of the transition is hence estimated to be ~0.55 at $g_x = 1$. Furthermore, from Fig. 7c, the core where substantial nonlocal effects take place spans roughly five to seven lattice sites which, as per the saturated value of $[R_\infty]$ in Fig. 7f, is comparable to a thermal segment of approximately three lattice-spacing long.

This embedded thermal-like core in IOMs plays a crucial role in yielding the novel Lieb-Robinson bound for cMBL. More relevant mathematical justifications are in ref. [58].

cMBL-dMBL transition and return probability

In view of the importance of core formation in driving the change between cMBL and dMBL, we perform a finite-size scaling analysis on 'dynamic order parameters' $[\varepsilon_{\rm res}]$ and $[R_\infty]$ to locate more precisely the critical value of W_z that triggers this eigenstate transition. Following ref. [68], the target quantity $Q = [\varepsilon_{\rm res}]$ (or $[R_\infty]$) at fixed g_x might assume a standard scaling form as follows, $\frac{Q(L,W_z)}{L^{\sigma_Q}} \approx f_Q\left((W_z - W_{z,Q}^c)L^{\alpha_Q}\right)$, where f_Q is some unknown function associated to Q and similarly σ_Q, α_Q are the corresponding scaling exponents. The critical strength $W_{z,Q}^c$ of the transition can then be extracted from the proper data collapse of Q.

Figure 8 depicts scaling profiles of $[\varepsilon_{\rm res}]$ and $[R_\infty]$ at fixed $g_x = 1$ for different system sizes ranging from $L = 11$ to 25 using PBCs. As shown by panel a, the scaling collapse of the data for $[\varepsilon_{\rm res}]$ yields the following set of parameters, $W_{z,\varepsilon}^c \approx 0.55$, $\sigma_\varepsilon \approx -0.01$, $\alpha_\varepsilon \approx 0.2$.

Although $[\varepsilon_{\rm res}]$ and $[R_\infty]$ carry compatible information, as $[\varepsilon_{i_c}(t)]$ stands for return probability, an autocorrelation function easier to measure in experiments, we extend its evaluation to longer chains $L = 23$, 25 by resorting to the Krylov-typicality technique (see methods section). Figure 9a presents the obtained $[\varepsilon_{\frac{L+1}{2}}(t)]$ for a range of W_z close to the transition of $g_x = 1$. It is noticeable that due to localization, all evolution curves relax to their constant lineshapes whose saturation values enhance with W_z and form two individual plateaus around ~0.45 for cMBL and ~1 for dMBL, respectively. This convergent trend allows for an estimate of $[\varepsilon_{\rm res}]$ by averaging the return probability over a later period $t \in [1000, 2000]$, which produces the data points of $L = 23$, 25 in Fig. 8a. The reliability of such a procedure is justified by Fig. 9b where we check the correctness of Krylov-typicality approximation and the appropriateness of the chosen time window via a benchmark test against the exact results of $L = 21$.

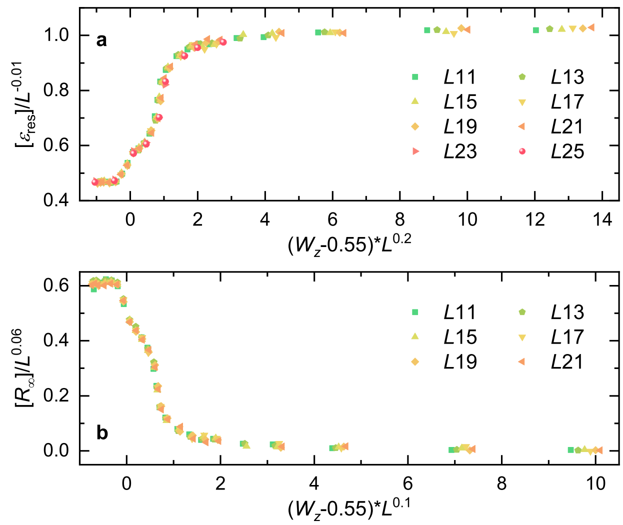

Fig. 8 Finite-size scaling analysis for cMBL-dMBL transition at fixed $g_x = 1$. The respective data collapse of random-averaged dynamic order parameters $[\varepsilon_{\rm res}]$ [panel **a**] and $[R_\infty]$ [panel **b**] yields consistently a critical $W_z^c \sim 0.55 W_x$. Here, PBCs are used; for $L = 23, 25$, the results are extracted from the Krylov-typicality approach; other sizes are solved by ED.

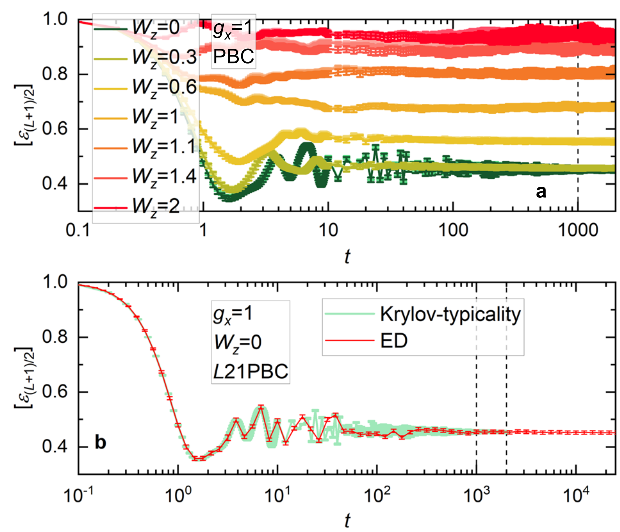

Fig. 9 Longer-chain results. a Time evolution of return probability as a function of W_z at fixed $g_x = 1$ obtained by applying the Krylov-typicality method to periodic chains. The light to solid colors give the results of $L = 21$, 23, 25. **b** A sample calculation on a small chain illustrates that Krylov-typicality approximation reproduces the results of ED.

Because energy diffusion is ceased in localized regions (in other words, the initial energy imbalance is restricted to the chain center), adding more sites on the chain ends generates small finite-size flows of $[\varepsilon_{\rm res}]$ seen in Fig. 8a, even after raising the length limit to $L = 25$. Likewise, as plotted in Fig. 8b, the estimates of scaling parameters obtained from the data collapse of $[R_\infty]$ read $W_{z,R}^c \approx 0.55$, $\sigma_R \approx 0.06$, $\alpha_R \approx 0.1$.

DISCUSSION

To conclude, we find a cMBL regime and a probably discontinuous cMBL-cETH transition in the quasirandom Rydberg-blockade chain. The orthogonality between the field and the projection directions renders cMBL and its discontinuous eigenstate transition fundamentally different from dMBL, uMBL, and the continuous uMBL-uETH transition. Particularly, the entanglement entropy in cMBL grows as a double-log function of time, as opposed to the power-law growth in dMBL and the single-log growth in uMBL.

The presumed discontinuity of the cMBL-cETH transition has been evidenced numerically. It is also possible to envision that a future analytical elucidation of its underpinnings may potentially improve the existing theoretical framework for MBL transition in a substantial way.

Even though LIOMs capture the phenomenology of dMBL, the cMBL-dMBL transition triggered by the rotation of the field orientation accentuates the importance of the nonlocal components in the IOMs of cMBL, which, together with the double-log entanglement growth, raises doubts about how to define the meaningful LIOMs and the universal Hamiltonian suitable for cMBL.

The continued investigations on these open questions might thus hold the prospect of furthering our understanding of the unconventional MBL beyond the current scope.

METHODS

Quantum dynamics computations

In this work, to cope with the many-body nonequilibrium problem subject to intertwining complexities from constraint and randomness, three numerical approaches, ED, Krylov-typicality, and TEBD, are employed.

For small chains, we resort to the ED method to access the long-time limit, where quadruple precision is implemented for achieving the time scale up to $t \approx 10^{29}$. Within full diagonalization, the infinite-time limit is resolvable by invoking the diagonal approximation. Further, rather than removing the $\downarrow\downarrow$-motifs from unconstrained Hilbert space, we construct the projected spin-$\frac{1}{2}$ basis as a selected set of binary numbers by fulfilling the constraint rule using combinatorial reasoning, which is more efficient for larger system sizes.

One alternative to evaluate the time evolution of longer quantum spin chains, albeit with the limitation of much shorter time scales, is the TEBD algorithm[70], which is built upon parametrization of a quantum wavefunction in terms of matrix-product states (MPS)[78],

$$|\psi\rangle = \sum_{\sigma_1,\dots,\sigma_L} A^{[1]}A^{[2]}\cdots A^{[L]}|\sigma_1,\dots,\sigma_L\rangle, \tag{15}$$

where $A^{[i]}$ stands for a three-leg tensor at site i carrying one physical bond $\sigma_i = 1, 2$ for a local spin-$\frac{1}{2}$ system and two virtual legs of dimension χ_L^i and χ_R^i. TEBD relies on the low amount of entanglement generation and the Suzuki-Trotter decomposition of the time evolution operator. Concretely, at fourth order, this unitary can be approximated in a symmetric format[78],

$$e^{-\mathrm{i}H\tau} = U(\tau_1)U(\tau_2)U(\tau_3)U(\tau_2)U(\tau_1) + \mathcal{O}(\tau^5), \tag{16}$$

where

$$U(\tau_i) = e^{-\mathrm{i}H_{\mathrm{odd}}\tau_i/2}e^{-\mathrm{i}H_{\mathrm{even}}\tau_i}e^{-\mathrm{i}H_{\mathrm{odd}}\tau_i/2}, \tag{17}$$

$$\tau_1 = \tau_2 = \frac{\tau}{4-\sqrt[3]{4}}, \quad \tau_3 = \tau - 2(\tau_1 + \tau_2), \tag{18}$$

and we assume that the total inspected Hamiltonian H comprises a sum of two-site operators that can be divided into the respective H_{even} and H_{odd} parts living across the even and odd bonds. Evidently, starting from an arbitrary product state in the projective spin basis, to a good approximation, the repeated application of the unitary time evolution will not generate components that violate the constraint.

The calculation of QFI entails the evaluation of I^2, which is easily computed within TEBD via recasting I as a matrix-product operator (MPO)[78]: analogous to the MPS representation in Eq. (15), a generic operator O is rewritten as

$$O = \sum_{\substack{\sigma_1,\dots,\sigma_L \\ \sigma'_1,\dots,\sigma'_L}} W^{[1]}W^{[2]}\cdots W^{[L]}|\sigma_1,\dots,\sigma_L\rangle\langle\sigma'_1,\dots,\sigma'_L|, \tag{19}$$

where $W^{[i]}$ is a four-leg tensor on site i equipped with two physical bonds σ_i, σ'_i and two virtual bonds of dimension $D \times D$. For spin-imbalance operator I, W's are simply given by

$$W^{[i]} = \begin{bmatrix} \mathbb{1} & f_i\sigma_i^z \\ 0 & \mathbb{1} \end{bmatrix}, \tag{20}$$

where $f_i = (-1)^i/L$, and $\mathbb{1}, \sigma_i^z$ are 2×2 Pauli matrices, therefore $D = 2$ in this case. Then, I^2 consists of a stacking of two identical layers of W's tensors, whose expectation value at t is obtained by executing optimal contractions.

For brevity, let us recap the main steps of the Krylov-space technique. By definition, starting from an arbitrary normalized wave-vector $|\phi_0\rangle$, the associated linearly-independent Krylov subspace $\mathcal{K}$ is generated by consecutively applying the Hamiltonian H onto $|\phi_0\rangle$ $(m-1)$ times,

$$\mathcal{K} := \left\{|\phi_0\rangle, H|\phi_0\rangle, H^2|\phi_0\rangle, \cdots, H^{m-1}|\phi_0\rangle\right\}. \tag{21}$$

Through clever recombination, an equivalent but more convenient reformulation of $\mathcal{K}$ exists, which is mutually orthonormal and called the Lanczos basis derived from $|\phi_0\rangle = |v_0\rangle$,

$$\mathcal{K} \sim \mathcal{L} := \{|v_0\rangle, |v_1\rangle, |v_2\rangle, \cdots, |v_{m-1}\rangle\}, \tag{22}$$

where, to remedy the loss of orthogonality, the procedure of reorthogonality is always assumed. The advantage of $\mathcal{L}$ lies in the fact that for most practical calculations, it suffices to choose the Lanczos dimension $m \approx 50$ to 100, which is orders of magnitude smaller than the full Hilbert-space dimension $\mathcal{D}$.

The above rationale can be recapitulated in terms of the following basis transformation,

$$F^\dagger H F = H_{\mathrm{lanc}}, \tag{23}$$

where the full Hamiltonian H is written in the original physical basis, while the heavily reduced Hamiltonian H_{lanc} is recast in the Lanczos basis specific for the neighborhood of $|v_0\rangle = |\phi_0\rangle$. It is easy to prove that for Hermitian operator H, H_{lanc} is a tridiagonal matrix. Moreover, stacking the Lanczos states yields the fundamental transformation matrices $F, F^\dagger$,

$$F = [|v_0\rangle|v_1\rangle|v_2\rangle\cdots|v_{m-1}\rangle]_{\mathcal{D}\times m}, \tag{24}$$

$$F^\dagger = \begin{bmatrix} \langle v_0| \\ \langle v_1| \\ \vdots \\ \langle v_{m-1}| \end{bmatrix}_{m\times\mathcal{D}}. \tag{25}$$

The essence of Lanczos approximation can then be encapsulated in terms of the following single relation,

$$FF^\dagger \approx \mathbb{1}_{m\times m}, \tag{26}$$

which is exact iff m equals the Hilbert-space dimension $\mathcal{D}$.

Armed with these preparations, we are ready to derive the formula for the real-time propagation of a normalized vector $|\psi(t)\rangle = |\phi_0\rangle = |v_0\rangle$ under the unitary evolution of the Hamiltonian H up to a small time decimation δ, i.e.,

$$|\psi(t+\delta)\rangle \approx F V_{\mathrm{lanc}} e^{-\mathrm{i}\frac{\delta}{\hbar}D_{\mathrm{lanc}}} V_{\mathrm{lanc}}^\dagger F^\dagger |\psi(t)\rangle, \tag{27}$$

where the tridiagonal Lanczos matrix H_{lanc} is diagonalized by the unitary matrix V_{lanc}, $H_{\mathrm{lanc}} = V_{\mathrm{lanc}} D_{\mathrm{lanc}} V_{\mathrm{lanc}}^\dagger$. Symbolically, one writes the combined vector $F^\dagger|\psi(t)\rangle$ in the explicit form,

$$F^\dagger|\psi(t)\rangle = \begin{bmatrix} \frac{\langle\psi(t)|\psi(t)\rangle}{\sqrt{\langle\psi(t)|\psi(t)\rangle}} \\ 0 \\ \vdots \\ 0 \end{bmatrix}_{m\times 1}, \tag{28}$$

where the zeros are resultant from the orthogonality between different Lanczos basis states.

Notice that both $|\psi(t)\rangle$ and $|\psi(t+\delta)\rangle$ are $\mathcal{D}\times 1$ vectors in the computational basis, therefore the evaluation of the half-chain von Neumann entanglement entropy at $t+\delta$ is proceeded in the usual way once $|\psi(t+\delta)\rangle$ is available.

For an initial energy inhomogeneity at the central site of a Rydberg chain, its return probability under the unitary time evolution of the quasiperiodic Hamiltonian $H_{\rm qp}$ is

$$\varepsilon_{\frac{L+1}{2}}(t) := \frac{1}{Tr\left[\widetilde{\rho}(t)H_{\rm qp}\right]} Tr\left[\widetilde{\rho}(t)H_{\frac{L+1}{2}}\right]. \tag{29}$$

Here we assume the infinite temperature. The initial density matrix $\widetilde{\rho}(t=0)$ specifies the spatial distribution of the energy disturbance at $t=0$, whose subsequent dynamics can be couched in the Heisenberg representation as ($\hbar=1$),

$$\widetilde{\rho}(t) := e^{iH_{\rm qp}t}\cdot\widetilde{\rho}(t=0)\cdot e^{-iH_{\rm qp}t}, \tag{30}$$

$$\widetilde{\rho}(t=0) := \frac{\varepsilon}{\mathcal{D}}\widetilde{X}_{\frac{L+1}{2}}. \tag{31}$$

Note that $H_{\rm qp}$ is discretized in Eq. (29), i.e.,

$$H_{\rm qp} = \sum_{i=1}^{L} H_i, \quad \text{where} \quad H_i = g_i\widetilde{X}_i + h_i\widetilde{Z}_i. \tag{32}$$

There exists one extra complication in the computation of $\varepsilon_{\frac{L+1}{2}}(t)$. By full diagonalization, the trace over the entire Hilbert space is accomplishable through summing up the contributions of all eigenvectors with the equal weight,

$$Tr[\dots] = \sum_{n=1}^{\mathcal{D}}\langle E_n|\dots|E_n\rangle. \tag{33}$$

This approach is impractical once $L\geqslant 23$. For instance, when $L=23$ under PBCs, $\mathcal{D}=64079$ and the required ram to compute a single random realization is over 190 GB.

To make progress, we invoke the trick of dynamical typicality[79–81] to approximately evaluate the trace of an operator over the gigantic Hilbert space. The key idea is to replace Eq. (33) by a single scalar product using a pure state $|\Psi_{\rm gaus}\rangle$,

$$\frac{1}{\mathcal{D}}Tr[\dots] = \frac{1}{\mathcal{D}}\sum_{n=1}^{\mathcal{D}}\langle E_n|\dots|E_n\rangle \approx \langle\Psi_{\rm gaus}|\dots|\Psi_{\rm gaus}\rangle, \tag{34}$$

where $|\Psi_{\rm gaus}\rangle$ is written in the computational basis with dimension $\mathcal{D}$ whose entries are Gaussian random numbers with zero means. The Gaussian distribution of the complex components of $|\Psi_{\rm gaus}\rangle$ guarantees that $|\Psi_{\rm gaus}\rangle$ is drawn uniformly on the hypersphere of the full Hilbert space (i.e., according to the Haar measure) such that the corresponding probability distribution is invariant under all unitary transformations within the Hilbert space. As per formal theory of typicality[79,80], $|\Psi_{\rm gaus}\rangle$ could be an effective representative of the underlying statistical ensemble.

Practically, $|\Psi_{\rm gaus}\rangle$ is constructed in a simple manner,

$$|\Psi_{\rm gaus}\rangle = \frac{1}{\mathcal{N}}\sum_{a=1}^{\mathcal{D}}(r_a + is_a)|a\rangle, \tag{35}$$

where $|a\rangle$ enumerates the physical computational basis, and r_a, s_a are real, independent Gaussian random numbers with mean zero and variance one, $\mathcal{N} = \sqrt{\sum_{a=1}^{\mathcal{D}}\left[r_a^2+s_a^2\right]}$. As $\mathcal{D}$ is at the order of 10^7 (for example, $\mathcal{D}=1346269$ for $L=29$ under OBCs), for averages over 2000 independent quasirandom realizations, a good random number generator with long period (~10^{18}) might be needed.

In real computation, the accuracy of dynamical typicality can be improved by using multiple pure Gaussian states in a single evaluation of Eq. (34). To maximize the overall landscape for the random realizations of $H_{\rm qp}$ and $|\Psi_{\rm gaus}\rangle$, it is economic to invoke one independent $|\Psi_{\rm gaus}\rangle$ for each different quasiperiodic $H_{\rm qp}$, and then perform the average over 2000 such joint samples. Accordingly, under the assumption of the validity of dynamical typicality, the random-averaged return probability might be approximated as follows,

$$[\varepsilon_{\frac{L+1}{2}}(t)] \approx \frac{1}{\mathcal{R}}\sum_{q=1}^{\mathcal{R}}\left\langle\Psi^q_{\rm gaus}\middle|\left[\widetilde{X}^q_{\frac{L+1}{2}}(t)\widetilde{X}_{\frac{L+1}{2}}\right]\middle|\Psi^q_{\rm gaus}\right\rangle, \tag{36}$$

where q denotes the involvement of the qth random sample and the total number for the joint random samples is over 2000, $\mathcal{R}\geqslant 2000$. Being a scalar product of the pure state, each summand in Eq. (36) is evaluable by the Lanczos method.

For all results presented in this paper, we perform the random sample calculations over at least 1000 independent quasiperiodic configurations of the model parameters ϕ_x, ϕ_z and when evaluating entanglement growth, the initial product states are additionally selected from the constrained spin basis in another randomized manner[73]. The corresponding statistical uncertainties are estimated from the normal variance of varied averaged quantities as per the procedure of ref. [62].

DATA AVAILABILITY

The data set that supports the findings of the present study can be available from the corresponding authors via email upon request.

Received: 30 September 2021; Accepted: 16 November 2022;
Published online: 03 December 2022

REFERENCES

1. Anderson, P. W. Absence of diffusion in certain random lattices. *Phys. Rev.* **109**, 1492 (1958).
2. Basko, D., Aleiner, I. & Altshuler, B. Metal-insulator transition in a weakly interacting many-electron system with localized single-particle states. *Ann. Phys.* **321**, 1126–1205 (2006).
3. Gornyi, I. V., Mirlin, A. D. & Polyakov, D. G. Interacting electrons in disordered wires: Anderson localization and low-*T* transport. *Phys. Rev. Lett.* **95**, 206603 (2005).
4. Deutsch, J. M. Quantum statistical mechanics in a closed system. *Phys. Rev. A* **43**, 2046 (1991).
5. Srednicki, M. Chaos and quantum thermalization. *Phys. Rev. E* **50**, 888 (1994).
6. Abanin, D. A., Altman, E., Bloch, I. & Serbyn, M. Colloquium: many-body localization, thermalization, and entanglement. *Rev. Mod. Phys.* **91**, 021001 (2019).
7. Nandkishore, R. & Huse, D. A. Many-body localization and thermalization in quantum statistical mechanics. *Annu. Rev. Condens. Matter Phys.* **6**, 15–38 (2015).
8. Turner, C. J., Michailidis, A. A., Abanin, D. A., Serbyn, M. & Papić, Z. Weak ergodicity breaking from quantum many-body scars. *Nat. Phys.* **14**, 745–749 (2018).
9. van Horssen, M., Levi, E. & Garrahan, J. P. Dynamics of many-body localization in a translation-invariant quantum glass model. *Phys. Rev. B* **92**, 100305 (2015).
10. Hickey, J. M., Genway, S. & Garrahan, J. P. Signatures of many-body localisation in a system without disorder and the relation to a glass transition. *J. Stat. Mech.* **2016**, P054047 (2016).
11. Pancotti, N., Giudice, G., Cirac, J. I., Garrahan, J. P. & Bañuls, M. C. Quantum east model: localization, nonthermal eigenstates, and slow dynamics. *Phys. Rev. X* **10**, 021051 (2020).
12. Smith, A., Knolle, J., Kovrizhin, D. L. & Moessner, R. Disorder-free localization. *Phys. Rev. Lett.* **118**, 266601 (2017).

13. Brenes, M., Dalmonte, M., Heyl, M. & Scardicchio, A. Many-body localization dynamics from gauge invariance. *Phys. Rev. Lett.* **120**, 030601 (2018).
14. Sierant, P., Delande, D. & Zakrzewski, J. Many-body localization due to random interactions. *Phys. Rev. A* **95**, 021601 (2017).
15. Li, X., Deng, D.-L., Wu, Y.-L. & Das Sarma, S. Statistical bubble localization with random interactions. *Phys. Rev. B* **95**, 020201 (2017).
16. Bar Lev, Y., Reichman, D. R. & Sagi, Y. Many-body localization in system with a completely delocalized single-particle spectrum. *Phys. Rev. B* **94**, 201116 (2016).
17. Ros, V., Müller, M. & Scardicchio, A. Integrals of motion in the many-body localized phase. *Nucl. Phys. B* **891**, 420–465 (2015).
18. Imbrie, J. Z., Ros, V. & Scardicchio, A. Local integrals of motion in many-body localized systems. *Ann. der Phys.* **529**, 1600278 (2017).
19. Serbyn, M., Papić, Z. & Abanin, D. A. Local conservation laws and the structure of the many-body localized states. *Phys. Rev. Lett.* **111**, 127201 (2013).
20. Huse, D. A., Nandkishore, R. & Oganesyan, V. Phenomenology of fully many-body-localized systems. *Phys. Rev. B* **90**, 174202 (2014).
21. Imbrie, J. Z. Diagonalization and many-body localization for a disordered quantum spin chain. *Phys. Rev. Lett.* **117**, 027201 (2016).
22. Bernien, H. et al. Probing many-body dynamics on a 51-atom quantum simulator. *Nature* **551**, 579–584 (2017).
23. Chen, C., Burnell, F. & Chandran, A. How does a locally constrained quantum system localize? *Phys. Rev. Lett.* **121**, 085701 (2018).
24. Šuntajs, J., Bonča, J., Prosen, T. & Vidmar, L. Quantum chaos challenges many-body localization. *Phys. Rev. E* **102**, 062144 (2020).
25. Šuntajs, J., Bonča, J., Prosen, T. & Vidmar, L. Ergodicity breaking transition in finite disordered spin chains. *Phys. Rev. B* **102**, 064207 (2020).
26. Panda, R. K., Scardicchio, A., Schulz, M., Taylor, S. R. & Žnidarič, M. Can we study the many-body localisation transition? *EPL* **128**, 67003 (2020).
27. Sierant, P., Delande, D. & Zakrzewski, J. Thouless time analysis of Anderson and many-body localization transitions. *Phys. Rev. Lett.* **124**, 186601 (2020).
28. Sierant, P., Lewenstein, M. & Zakrzewski, J. Polynomially filtered exact diagonalization approach to many-body localization. *Phys. Rev. Lett.* **125**, 156601 (2020).
29. Abanin, D. et al. Distinguishing localization from chaos: challenges in finite-size systems. *Ann. Phys.* **427**, 168415 (2021).
30. Sierant, P., Lazo, E. G., Dalmonte, M., Scardicchio, A. & Zakrzewski, J. Constraint-induced delocalization. *Phys. Rev. Lett.* **127**, 126603 (2021).
31. Mondaini, R. & Rigol, M. Many-body localization and thermalization in disordered Hubbard chains. *Phys. Rev. A* **92**, 041601 (2015).
32. Luitz, D. J., Laflorencie, N. & Alet, F. Many-body localization edge in the random-field Heisenberg chain. *Phys. Rev. B* **91**, 081103 (2015).
33. Kiefer-Emmanouilidis, M., Unanyan, R., Fleischhauer, M. & Sirker, J. Evidence for unbounded growth of the number entropy in many-body localized phases. *Phys. Rev. Lett.* **124**, 243601 (2020).
34. Luitz, D. J. & Lev, Y. B. Absence of slow particle transport in the many-body localized phase. *Phys. Rev. B* **102**, 100202 (2020).
35. Kiefer-Emmanouilidis, M., Unanyan, R., Fleischhauer, M. & Sirker, J. Slow delocalization of particles in many-body localized phases. *Phys. Rev. B* **103**, 024203 (2021).
36. Sels, D. & Polkovnikov, A. Dynamical obstruction to localization in a disordered spin chain. *Phys. Rev. E* **104**, 054105 (2021).
37. Vidmar, L., Krajewski, B., Bonča, J. & Mierzejewski, M. Phenomenology of spectral functions in disordered spin chains at infinite temperature. *Phys. Rev. Lett.* **127**, 230603 (2021).
38. Morningstar, A., Colmenarez, L., Khemani, V., Luitz, D. J. & Huse, D. A. Avalanches and many-body resonances in many-body localized systems. *Phys. Rev. B* **105**, 174205 (2022).
39. Iyer, S., Oganesyan, V., Refael, G. & Huse, D. A. Many-body localization in a quasiperiodic system. *Phys. Rev. B* **87**, 134202 (2013).
40. Khemani, V., Sheng, D. N. & Huse, D. A. Two universality classes for the many-body localization transition. *Phys. Rev. Lett.* **119**, 075702 (2017).
41. Lee, M., Look, T. R., Lim, S. P. & Sheng, D. N. Many-body localization in spin chain systems with quasiperiodic fields. *Phys. Rev. B* **96**, 075146 (2017).
42. Nag, S. & Garg, A. Many-body mobility edges in a one-dimensional system of interacting fermions. *Phys. Rev. B* **96**, 060203 (2017).
43. Dutta, A., Mukerjee, S. & Sengupta, K. Many-body localized phase of bosonic dipoles in a tilted optical lattice. *Phys. Rev. B* **98**, 144205 (2018).
44. Zhang, S.-X. & Yao, H. Universal properties of many-body localization transitions in quasiperiodic systems. *Phys. Rev. Lett.* **121**, 206601 (2018).
45. Agrawal, U., Gopalakrishnan, S. & Vasseur, R. Universality and quantum criticality in quasiperiodic spin chains. *Nat. Commun.* **11**, 2225 (2020).
46. Macé, N., Laflorencie, N. & Alet, F. Many-body localization in a quasiperiodic Fibonacci chain. *SciPost Phys.* **6**, 50 (2019).
47. Singh, H., Ware, B., Vasseur, R. & Gopalakrishnan, S. Local integrals of motion and the quasiperiodic many-body localization transition. *Phys. Rev. B* **103**, L220201 (2021).
48. Duthie, A., Roy, S. & Logan, D. E. Localization in quasiperiodic chains: a theory based on convergence of local propagators. *Phys. Rev. B* **104**, 064201 (2021).
49. Sierant, P. & Zakrzewski, J. Level statistics across the many-body localization transition. *Phys. Rev. B* **99**, 104205 (2019).
50. Aramthottil, A. S., Chanda, T., Sierant, P. & Zakrzewski, J. Finite-size scaling analysis of the many-body localization transition in quasiperiodic spin chains. *Phys. Rev. B* **104**, 214201 (2021).
51. Thomson, S. J. and Schiró, M. Local Integrals of motion in quasiperiodic many-body localized systems. Preprint at https://arxiv.org/abs/2110.02906 (2021).
52. Žnidarič, M. & Ljubotina, M. Interaction instability of localization in quasiperiodic systems. *Proc. Natl Acad. Sci. USA* **115**, 4595–4600 (2018).
53. Szabó, A. & Schneider, U. Mixed spectra and partially extended states in a two-dimensional quasiperiodic model. *Phys. Rev. B* **101**, 014205 (2020).
54. Doggen, E. V. H. & Mirlin, A. D. Many-body delocalization dynamics in long Aubry-André quasiperiodic chains. *Phys. Rev. B* **100**, 104203 (2019).
55. Sierant, P. & Zakrzewski, J. Challenges to observation of many-body localization. *Phys. Rev. B* **105**, 224203 (2022).
56. Khemani, V., Laumann, C. R. & Chandran, A. Signatures of integrability in the dynamics of Rydberg-blockaded chains. *Phys. Rev. B* **99**, 161101 (2019).
57. Huse, D. A., Nandkishore, R., Oganesyan, V., Pal, A. & Sondhi, S. L. Localization-protected quantum order. *Phys. Rev. B* **88**, 014206 (2013).
58. Chen, C., Chen, Y. and Wang, X. Lieb-Robinson bound for constrained many-body localization. Preprint at https://arxiv.org/abs/2011.11363 (2020).
59. Schreiber, M. et al. Observation of many-body localization of interacting fermions in a quasirandom optical lattice. *Science* **349**, 842–845 (2015).
60. Bordia, P. et al. Coupling identical one-dimensional many-body localized systems. *Phys. Rev. Lett.* **116**, 140401 (2016).
61. Lukin, A. et al. Probing entanglement in a many-body-localized system. *Science* **364**, 256–260 (2019).
62. Oganesyan, V. & Huse, D. A. Localization of interacting fermions at high temperature. *Phys. Rev. B* **75**, 155111 (2007).
63. Atas, Y. Y., Bogomolny, E., Giraud, O. & Roux, G. Distribution of the ratio of consecutive level spacings in random matrix ensembles. *Phys. Rev. Lett.* **110**, 084101 (2013).
64. Giraud, O., Macé, N., Vernier, E. & Alet, F. Probing symmetries of quantum many-body systems through gap ratio statistics. *Phys. Rev. X* **12**, 011006 (2022).
65. De Roeck, W. & Huveneers, F. Stability and instability towards delocalization in many-body localization systems. *Phys. Rev. B* **95**, 155129 (2017).
66. Yu, X., Luitz, D. J. & Clark, B. K. Bimodal entanglement entropy distribution in the many-body localization transition. *Phys. Rev. B* **94**, 184202 (2016).
67. Page, D. N. Average entropy of a subsystem. *Phys. Rev. Lett.* **71**, 1291 (1993).
68. Kjäll, J. A., Bardarson, J. H. & Pollmann, F. Many-body localization in a disordered quantum ising chain. *Phys. Rev. Lett.* **113**, 107204 (2014).
69. Khemani, V., Lim, S. P., Sheng, D. N. & Huse, D. A. Critical properties of the many-body localization transition. *Phys. Rev. X* **7**, 021013 (2017).
70. Vidal, G. Efficient simulation of one-dimensional quantum many-body systems. *Phys. Rev. Lett.* **93**, 040502 (2004).
71. Smith, J. et al. Many-body localization in a quantum simulator with programmable random disorder. *Nat. Phys.* **12**, 907–911 (2016).
72. Žnidarič, M., Prosen, T. & Prelovšek, P. Many-body localization in the Heisenberg *XXZ* magnet in a random field. *Phys. Rev. B* **77**, 064426 (2008).
73. Bardarson, J. H., Pollmann, F. & Moore, J. E. Unbounded growth of entanglement in models of many-body localization. *Phys. Rev. Lett.* **109**, 017202 (2012).
74. Serbyn, M., Papić, Z. & Abanin, D. A. Universal slow growth of entanglement in interacting strongly disordered systems. *Phys. Rev. Lett.* **110**, 260601 (2013).
75. Luitz, D. J., Laflorencie, N. & Alet, F. Extended slow dynamical regime close to the many-body localization transition. *Phys. Rev. B* **93**, 060201 (2016).
76. Kim, H. & Huse, D. A. Ballistic spreading of entanglement in a diffusive non-integrable system. *Phys. Rev. Lett.* **111**, 127205 (2013).
77. Chandran, A., Kim, I. H., Vidal, G. & Abanin, D. A. Constructing local integrals of motion in the many-body localized phase. *Phys. Rev. B* **91**, 085425 (2015).
78. Schollwöck, U. The density-matrix renormalization group in the age of matrix product states. *Ann. Phys.* **326**, 96–192 (2011).
79. Popescu, S., Short, A. J. & Winter, A. Entanglement and the foundations of statistical mechanics. *Nat. Phys.* **2**, 754–758 (2006).
80. Goldstein, S., Lebowitz, J. L., Tumulka, R. & Zanghì, N. Canonical typicality. *Phys. Rev. Lett.* **96**, 050403 (2006).
81. Steinigeweg, R., Herbrych, J., Pollmann, F. & Brenig, W. Typicality approach to the optical conductivity in thermal and many-body localized phases. *Phys. Rev. B* **94**, 180401 (2016).

ACKNOWLEDGEMENTS

The discussion with M. Heyl was acknowledged. We thank R. Boyack for a critical reading of the paper. We also thank the anonymous referees, whose suggestions and questions improve the manuscript a lot. C.C. was supported by a start-up fund from Shanghai Jiao Tong University. X.W. was supported by MOST2022YFA1402701 and the NSFC Grant No. 11974244. Y.C. was supported by the SKP of China Grant No. 2022YFA1404204 and the NSFC Grant No. 12274086.

AUTHOR CONTRIBUTIONS

All authors contributed equally to this work. C.C., X.W., and Y.C. conceived the project. C.C. performed the numerical and analytical calculations. All authors worked on the interpretation of the results and contributed to the writing of the manuscript.

COMPETING INTERESTS

The authors declare no competing financial or non-financial interests.

ADDITIONAL INFORMATION

Supplementary information The online version contains supplementary material available at https://doi.org/10.1038/s41534-022-00654-9.

Correspondence and requests for materials should be addressed to Chun Chen, Yan Chen or Xiaoqun Wang.